SANDIA REPORT
SAND2017-0056
Printed January 2017

Reduced Dimensionality Lithium Niobate Microsystems

Matt Eichenfield

Prepared by
Sandia National Laboratories
Albuquerque, New Mexico 87185 and Livermore, California 94550

Sandia National Laboratories is a multi-mission laboratory managed and operated by Sandia Corporation, a wholly owned subsidiary of Lockheed Martin Corporation, for the U.S. Department of Energy's National Nuclear Security Administration under contract DE-AC04-94AL85000.

Issued by Sandia National Laboratories, operated for the United States Department of Energy by Sandia Corporation.

SAND2017-0056
Printed January 2017

Reduced Dimensionality Lithium Niobate Microsystems

Matt Eichenfield
1719
Sandia National Laboratories
P.O. Box 5800
Albuquerque, New Mexico 87185-MS1080

Abstract

The following report describes work performed under the LDRD program at Sandia National Laboratories October 2014 and September 2016. The work presented demonstrates the ability of Sandia Labs to develop state-of-the-art photonic devices based on thin film lithium niobate ($LiNbO_3$). Section 1 provides an introduction to integrated $LiNbO_3$ devices and motivation for developing thin film nonlinear optical systems. Section 2 describes the design, fabrication, and photonic performance of thin film optical microdisks fabricated from bulk $LiNbO_3$ using a bulk implantation method developed at Sandia. Sections 3 and 4 describe the development of similar thin film $LiNbO_3$ structures fabricated from $LiNbO_3$ on insulator (LNOI) substrates and our demonstration of optical frequency conversion with state-of-the-art efficiency. Finally, Section 5 describes similar microdisk resonators fabricated from LNOI wafers with a buried metal layer, in which we demonstrate electro-optic modulation.

CONTENTS

FIGURES

1. INTRODUCTION

The following report describes work performed under the Laboratory Directed Research and Development (LDRD) program at Sandia National Laboratories between October 2014 and September 2016. The material chosen highlights the ability of Sandia National Labs to develop new technology platforms for state-of-the-art photonic devices. In particular, we describe our work with thin film lithium niobate ($LiNbO_3$) and our demonstration of efficient, low power, chip-scale optical frequency synthesis, as well as electro-optic modulation.

Efficient, chip-scale optical frequency synthesis at low power is essential for miniaturization and integration of photonic and quantum-optical systems. The development of precise frequency references, for example, typically requires second harmonic generation for self-referencing in octave spanning combs [1,2]; however, the available laser power and the low efficiency of the cascaded conversion processes required to generate the comb typically limit the power available in a single comb line to less than 1mW [3]. Efficient harmonic generation at very low powers is therefore a critical component for producing on-chip frequency references. Chip-scale frequency synthesis also provides an important tool for quantum information processing. Quantum memories, as well as single photon sources and detectors, often operate at visible wavelengths, where optical fiber losses are high [4]. Optical frequency conversion at the single photon level can provide a link between the visible and the near infrared for quantum systems, allowing these technologies to take advantage of low-loss transmission in optical fibers [5]. Nonlinear frequency conversion also provides a stable method for generating entangled photons [6]. Integrated entangled photon generation has so far been limited to low efficiency four wave mixing processes [7-9], or large foot-print periodically poled lithium niobate (PPLN) waveguides [10,11]. Highly efficient three wave mixing in a micron-scale resonator represents a significant improvement in size, weight, and power for entangled photon generation.

In this report, we describe a method for phase matching nonlinear optical interactions in chip-scale photonic architectures, as well as our efforts to develop fabrication techniques for thin film lithium niobate. Our approach exploits a sub-wavelength thickness dielectric film and differing electromagnetic boundary conditions for orthogonal polarizations for the pump and signal. Using this method, we achieve robust dispersion compensation at room temperature, removing a primary obstacle to efficient optical frequency synthesis in integrated devices. We demonstrate phase-matched, doubly resonant second harmonic generation (SHG) and spontaneous parametric down conversion (SPDC) in thin film lithium niobate ($LiNbO_3$) microresonators, achieving efficient optical frequency conversion at extremely low powers in a microfabricated system built with completely scalable fabrication techniques.

$LiNbO_3$ is an important material in nonlinear optics; its wide optical transparency window (350 nm – 5 μm) and large nonlinear susceptibility (d_{33} = 31.5pm/V, d_{31} = 4.5pm/V) have led to its ubiquity in optical frequency conversion in bulk optics [12]. In miniaturized $LiNbO_3$ systems, there have been many reports of frequency conversion experiments in high Q, mm-scale $LiNbO_3$ whispering gallery resonators [13-17], including demonstrations of high conversion efficiency for SHG [13,14] and spontaneous parametric down conversion (SPDC) [18] at low pump

powers. However, processing required to achieve a high quality surface finish (e.g. hand polishing) poses challenges for integration and further miniaturization of these devices.

The recent availability of single crystal $LiNbO_3$ as a sub-micron thickness film on top of a dielectric layer ($LiNbO_3$ on insulator, or LNOI) or on silicon has enabled high Q, micron-scale disk resonators [19-23]. There have been reports of SHG in several thin film $LiNbO_3$ microdisks [20-22], as well as microfabricated devices in other material systems [24-26]. A recent demonstration of aluminum nitride microring resonators with an SHG conversion efficiency of 2.5%/mW [27], as well an *ab initio* study by Johnson et al that predicts highly efficient doubly resonant frequency conversion in similar systems [28], suggest that imperfect phase matching may be responsible for limiting the performance of many of these devices, as achieved conversion efficiencies have been far less than the predicted maximum efficiencies based on the achieved system parameters such as resonator quality factors and mode volumes.

Our design uses birefringence and geometric dispersion [29] in thin films to achieve phase matching. We compensate for both normal material and normal resonator mode dispersion by exploiting the different electromagnetic boundary conditions for orthogonally polarized resonator modes. Using this novel method, which we refer to as geometric birefringent phase matching (gBPM), we show phase matched SHG and SPDC in 190 nm thick microdisks. We demonstrate SHG between fundamental resonator modes at 1544 nm and 772 nm, without periodic poling, with an internal conversion efficiency of 7.2% at 3mW of pump power. Although the signal power is not simply a quadratic function of pump power, this corresponds to approximately 2.4%/mW, nearly identical to the conversion efficiency reported in Ref 27. In contrast with Ref 27, we achieve this result without adjusting the temperature to dynamically adjust phase matching. We also emphasize that our method does not rely on modal dispersion of high-order resonator modes, achieving perfect phase matching using fundamental modes for both the pump and signal; this approach could provide advantages for future systems by, for example, taking advantage of better coupling to on-chip waveguide modes than would be possible with higher order modes.

In addition to SHG, we also demonstrate SPDC from 772 nm to 1544 nm in the same microdisk, capitalizing on the reversed interaction made possible with the same phase matching technique. The observed pair production rate of 27 kHz/μW is comparable to previously published figures in millimeter scale lithium niobate resonators, but because our production rate is so greatly enhanced by the reduced mode volumes, we can achieve this rate with a much lower quality factor.

In the following sections we provide detailed explanations of two separate methods for producing suspended thin film structures in $LiNbO_3$, as well as our demonstrations of efficient optical frequency synthesis and electro-optic modulation. The section describes a method for producing suspended thin film LiNbO3 microdisks using ion implantation of a bulk wafer. We also describe the optical performance of these devices and their potential applications in nonlinear optics. The second section details our work with commercially available LiNbO3 on insulator (LNOI) wafers. We discuss our experimental demonstrations of SHG and SPDC with state of the art efficiency using gBPM in $LiNbO_3$ microdisk resonators. The third section outlines

our work to create electro-optic modulators using similar microdisks fabricated from LNOI with a buried metal layer.

2. ION IMPLANTATION FOR LITHIUM NIOBATE PHOTONICS

Our fabrication approach is based on ion-implantation of a bulk $LiNbO_3$ wafer to achieve thin, suspended optical structures with much higher photonic performance than previously reported in bulk $LiNbO_3$ micromachining. The structures are fabricated using semiconductor processing techniques, without the use of high temperature reflow. This process represents an alternative to layer transfer methods, capable of producing high quality thin film $LiNbO_3$ photonic devices without heterogeneous integration. We use this process to produce thin film $LiNbO_3$ microdisks, with measured optical quality factors greater than 45,000 in the telecom band.

2.1 Micromachining Process

Our fabrication process for suspended microstructures in $LiNbO_3$ is based on an ion implantation of a bulk wafer. Patterning and etching through to the surface layer to a buried, ion-damaged layer defines the structures. The structures are then released by undercut etching, which selectively attacks the ion-damaged layer.

Fabrication steps are depicted in Figure 1. A z-cut $LiNbO_3$ wafer is implanted with 350 keV, 1.0e16 cm^2 dose of He, creating a buried layer of damaged $LiNbO_3$. A Cr/Si (500A/2000A) protect layer is used to protect the wafer surface and control the penetration depth of the ions. A SiO_2 hard mask prevents implantation in areas that will become support posts.

Cr, Si, and $LiNbO_3$ are patterned with a second oxide hard mask and dry etched to define the structures. Cr and Si are then removed. Finally, etching in HF undercuts into the ion-damaged $LiNbO_3$, releasing the structures.

Microdisks were fabricated with diameters ranging from 10-25μm, with final thickness measured by scanning electron microscopy from 165-400nm.

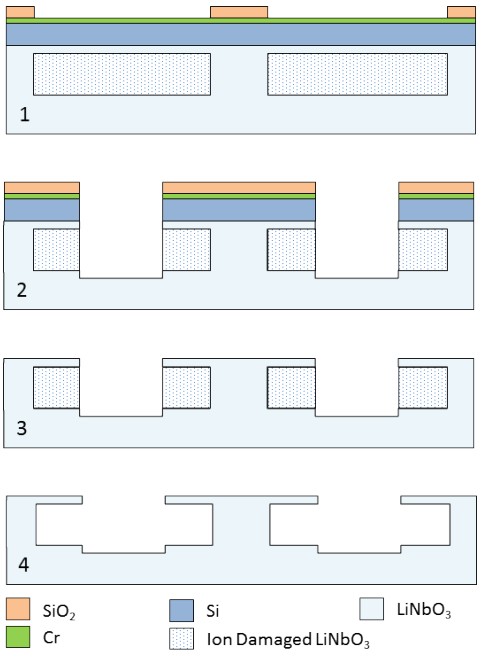

Figure 1. Process Flow for Suspended $LiNbO_3$ Structures

Figure 2 shows microscope and SEM images of a microdisk resonator fabricated with this process. Mcirodisks were fabricated with a range of diameters (10-25µm) and thicknesses (165-400nm). Optical characterization of microdisks is discussed in the next section.

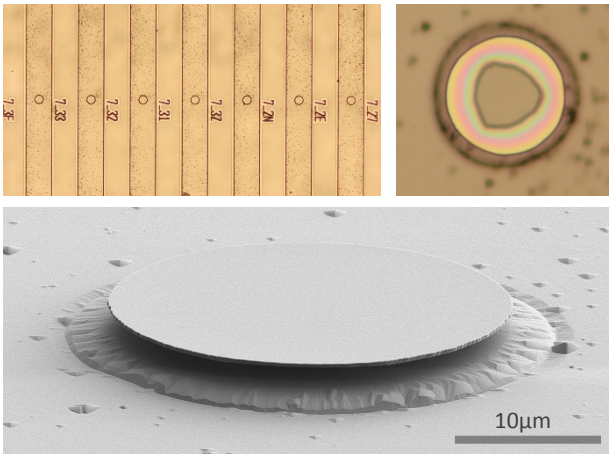

Figure 2. $LiNbO_3$ Thin Film Microdisks

2.2 Optical Characterization of Microdisks

Fabricated microdisks are probed with a tapered optical fiber. A standard SMF-28 fiber is stretched over a hydrogen flame, reducing its diameter to approximately 1µm over a transition region of several millimeters. The taper transitions adiabatically index guided to air-clad, remaining single mode over our laser bandwidth (1480-1640nm). In the narrow tapered region, laser light is no longer completely confined inside the fiber and propagates partially in the air. When the edge of the microdisk is placed near the taper, light evanescently couples to whispering gallery modes of the disk.

The tapered region of the coupler is "dimpled" by pressing it against a cylindrical mold and annealing, creating a bend. This allows the coupler to more easily approach the disks, which are only a few microns tall, while remaining physically separated from the chip surface and edges. Figure 3 shows a schematic and photograph of the measurement apparatus, as well as micrographs of the dimpled taper and microdisk. A similar tapered fiber was fabricated from 780HP fiber for characterization from 765-783nm and 830-853nm.

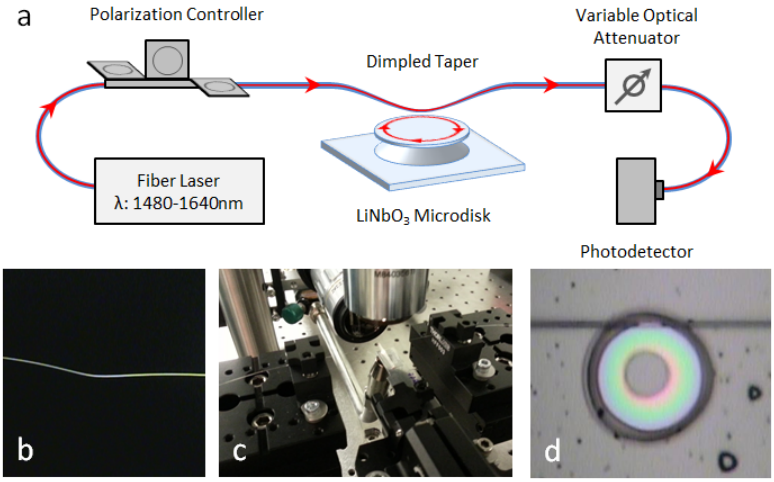

Figure 3. Tapered Fiber Coupler

The taper coupler is placed in close proximity to each microdisk, and the probe laser wavelength is tuned between 1480 and 1640nm to couple to whispering gallery modes of the disk [citation?]. The transmission spectrum for a 15µm diameter, 200nm thick microdisk is shown in Figure 4a. The free spectral range of the disk is approximately 2THz, or 17nm at 1550nm, and so the transmission spectrum in Fig. 4 includes several higher radial order modes. However, microdisks thinner than approximately 400 nm support only radially polarized (TE) modes of fundamental polar order.

The intrinsic (unloaded) quality factor Q_0 of each disk mode is extracted from a Lorentzian fit of the transmission spectrum (Fig. 4b). Typical intrinsic quality factors for modes our fabricated

microdisks in the 1550nm wavelength range are 20,000-40,000, with the highest measured Q_0 = 45,300. This corresponds to a finesse of approximately 500.

Q_0 was found to be lower for shorter wavelengths. The highest measured intrinsic quality factors for the 850nm and 775nm wavelength ranges were Q_0 = 37,100 and Q_0 = 3,560, respectively. We attribute this dependence of Q_0 on wavelength to increased scattering from surface defects at shorter wavelengths.

In contrast with prior work, the reported optical quality factors were achieved using only standard etching techniques and without the use of high temperature surface reflow.

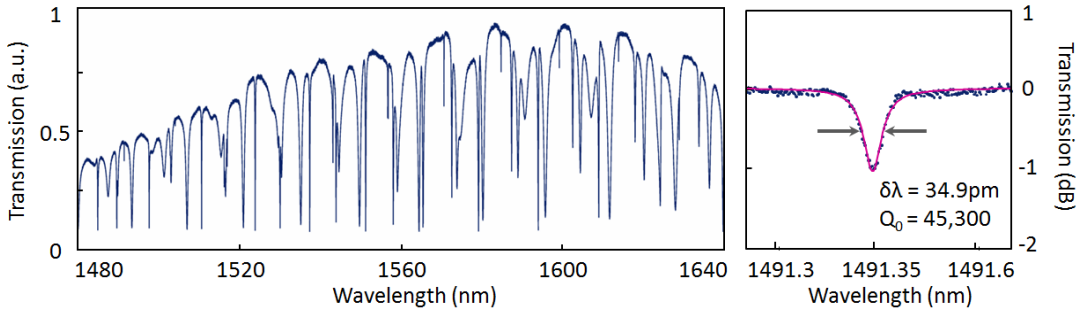

Figure 4. Transmission Spectrum and Quality Factor Measurement for $LiNbO_3$ Microdisk

2.3 Discussion

Although this fabrication process is capable of producing thin film photonic structures from bulk $LiNbO_3$, there remain challenges for the development of high performance integrated devices in this platform. In particular, optical scattering from surface roughness remains a limitation in our implanted film microdisks. This source of optical loss degrades the device quality factors and represents the primary obstacle to achieving highly efficient nonlinear optical systems in these films.

In the following sections, we discuss an alternate approach based on commercial $LiNbO_3$ on insulator (LNOI) wafers. Although this process relies on more expensive substrates, the devices produced from this material show much lower surface roughness and correspondingly higher optical quality factors. We show that when the optical quality of the $LiNbO_3$ films is increased, state of the art optical frequency conversion can be achieved in a chip-scale $LiNbO_3$ system.

3. LITHIUM NIOBATE ON INSULATOR (LNOI)

3.1 Introduction and Motivation

This section describes the development of a system for efficient optical frequency conversion based on chip-scale, thin film $LiNbO_3$ structures. We use commercial $LiNbO_3$ on insulator (LNOI) substrates, which consist of a think $LiNbO_3$ film on top of a 2 μm layer of silicon oxide, to produce suspended microdisk resonators. Although the wafers are more expensive than the bulk substrates used in the previous section, microdisks produced using this process show greatly reduced surface roughness, with a resulting increase in optical performance.

Using these microdisks, we develop a novel method for phase matching nonlinear optical interactions which relies on properties unique to thin film devices. We demonstrate optical frequency conversion with state of the art efficiency in these devices.

3.2 Design and Fabrication

Geometric Birefringent Phase Matching

Efficient nonlinear frequency conversion requires the interacting photons to satisfy specific relative phase requirements [30]. Momentum and energy conservation for doubly resonant SHG (and SPDC) in an azimuthally symmetric resonator require that:

$$2 \times m_1 - m_2 = \Delta m = 0 \tag{1}$$

$$2 \times f_1 - f_2 = \Delta f = 0 \quad (2 \times \lambda_2 - \lambda_1 = \Delta\lambda = 0) \tag{2}$$

with identical expressions for degenerate SPDC. m_1 and m_2 are the eigenvalues of angular momentum of the pump and second harmonic (SH) resonator modes, respectively, and f_1 and f_2 are the resonant eigenfrequencies of the pump and SH mode, respectively. Δm and Δf ($\Delta\lambda$) represent momentum and energy mismatch between the pump and SH modes, and are zero for perfect phase matching.

Eq. 1 and 2 are would not typically be simultaneously satisfied in our system for two reasons: First, since $LiNbO_3$ exhibits normal material dispersion ($n_1 < n_2$), doubling m will less-than-double f for modes confined in the disk. Second, our disks also exhibit normal geometric dispersion. This arises since the disks have sub-wavelength thickness, and the longer wavelength pump mode extends more outside the microdisk than the SH mode. The SH mode therefore has a lower effective index ($n_{1,eff} < n_{2,eff}$). In our devices, geometric dispersion is stronger than material dispersion, leading to $\Delta f >> 0$.

Selecting orthogonal polarizations for the pump and SH, however, can provide a solution to the phase matching problem. For a disk much thinner than both wavelengths, a significant fraction of

the energies for both the pump and SH modes are forced into the air, reducing their effective refractive indices. Because of the different electromagnetic boundary conditions for light polarized perpendicular (TM) and parallel (TE) to the substrate, TM modes are more strongly affected than TE modes, as depicted in Fig. 6. We show here that this geometric birefringence is strong enough to compensate for both normal material dispersion *and* normal geometric dispersion to achieve perfect phase matching in thin film $LiNbO_3$ microdisks.

Figure 6 outlines geometric birefringent phase matching (gBPM) for SHG in thin film microdisks. An azimuthally symmetric, 2D Finite element method simulation (Fig. 5,6) is used to determine the eigenfrequencies, f_1 and f_2, for the pump and SH modes of disks with varying geometries and m_1/m_2 pairs.

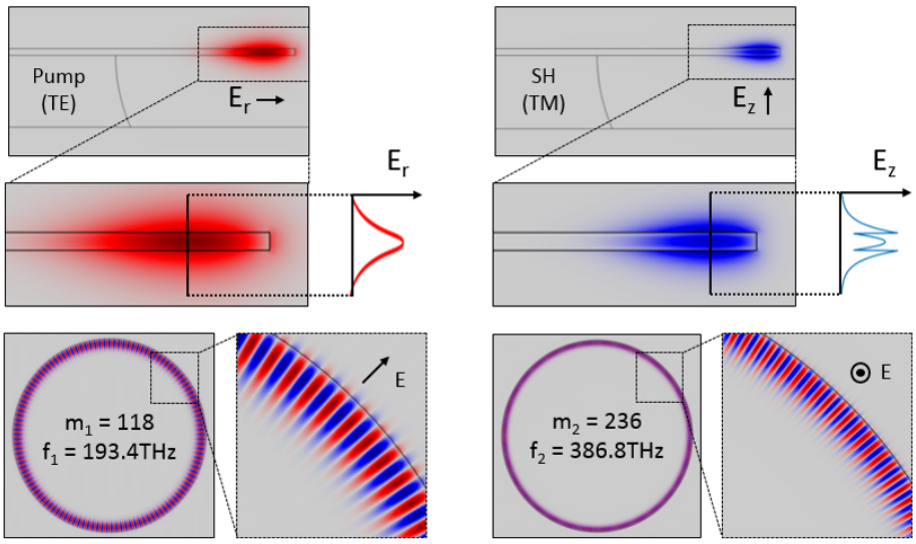

Figure 5. FEM Simulations for Microdisk Resonators

We first choose a target disk thickness near 200 nm. We simulate microdisks with varying radii and m_1/m_2 pairs that satisfy Eq. 1. For each m_1/m_2 pair, we calculate f_1 and f_2 for each polarization as a function of thickness. We adjust the radius and repeat the process until we identify a pump and SH mode which 1) satisfy Eq. 2 and 2) are inside our desired optical frequency ranges. The results for a particular case are plotted in Fig. 6. The TE pump mode and a TM SH mode are phase matched (f_1 = 193.41 THz, f_2 = 386.83 THz; m_1 =118, m_2 = 236) at a thickness of 190 nm and a radius of 20.62 μm. More details of the gBPM method, including discussion of compensation for film thickness variation, are provided in the next section.

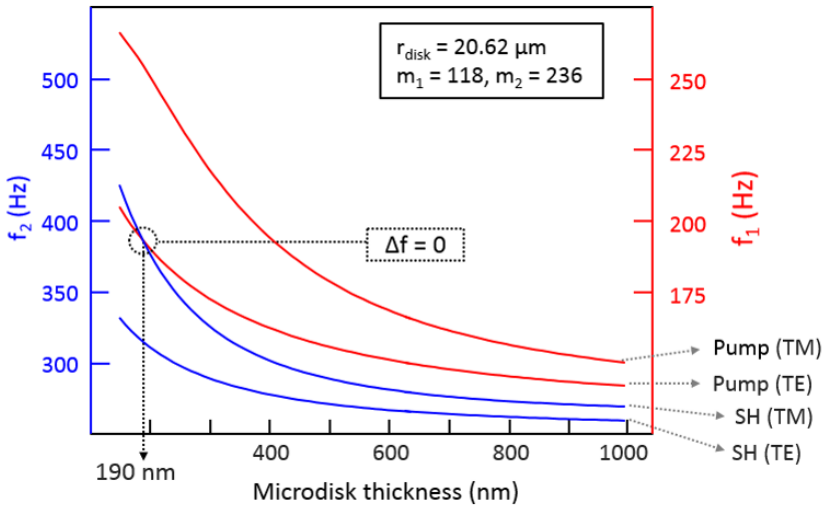

Figure 6. Geometric Birefringent Phase Matching for Microdisk Resonators

Microdisk Fabrication and Characterization

Figure 7 shows a simplified fabrication procedure for LNOI microdisks, as well as optical and scanning electron micrographs of completed disks. Microdisks were produced with radii varying from 10 to 27.5 µm and thicknesses from 180 to 200 nm. We fabricate an array of microdisks with the nominal radius stepped by 12 nm, in order to account for variations in thickness and radius due to processing.

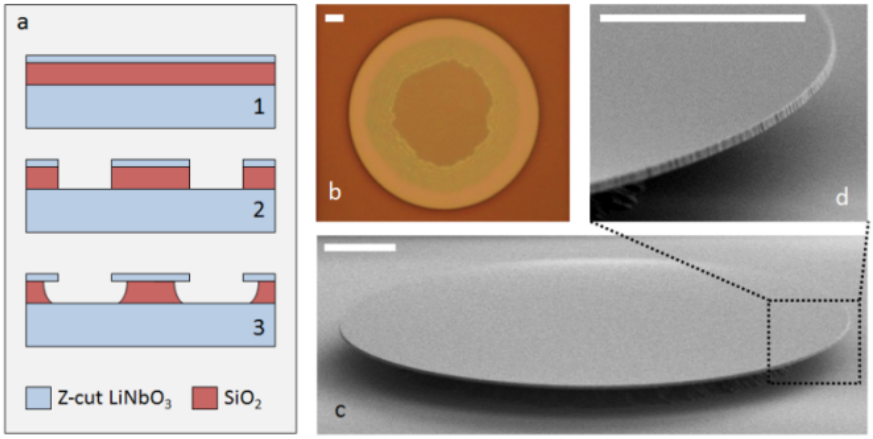

Figure 7. $LiNbO_3$ Microdisk Resonators

A tapered fiber probe [26,31,32] was used to couple light into and out of the disks (Fig. 8). The highest intrinsic (unloaded) optical quality factors measured were 570,000 for the 1550 nm wavelength range and 75,500 for the 775 nm wavelength range.

In order to experimentally verify phase matching, transmission spectra were recorded at the pump and signal wavelength ranges (Fig. 8) for a microdisk thickness 189.4 nm and radius 20.016μm using a single tapered fiber [26]. Laser wavelengths were recorded using a wave meter with resolution of 150 (200) MHz at 1550 (775) nm, ensuring accuracy of the spectral overlap of the resonator modes to ¼ of the loaded pump linewidth. In order to determine m_1 and m_2, the measured transmission spectra were compared with FEM simulations, described in the previous section. The measured mode wavelengths (λ_1 = 1544.15, λ_2 = 772.075) and deduced azimuthal mode numbers (m_1 = 121, m_2 = 242) match the FEM simulated values for our actual disk geometry, and satisfy the phase matching requirements in Eq. 1 and 2. We note that we cannot determine m to better than ± 1, due to limited precision in measuring the geometry and refractive index of the microdisks. However, this uncertainty results only in a slight shift of the optical frequencies, and so the phase matching process is robust to this limitation, provided that the frequency conversion remains in the desired frequency window.

3.3 Second Harmonic Generation

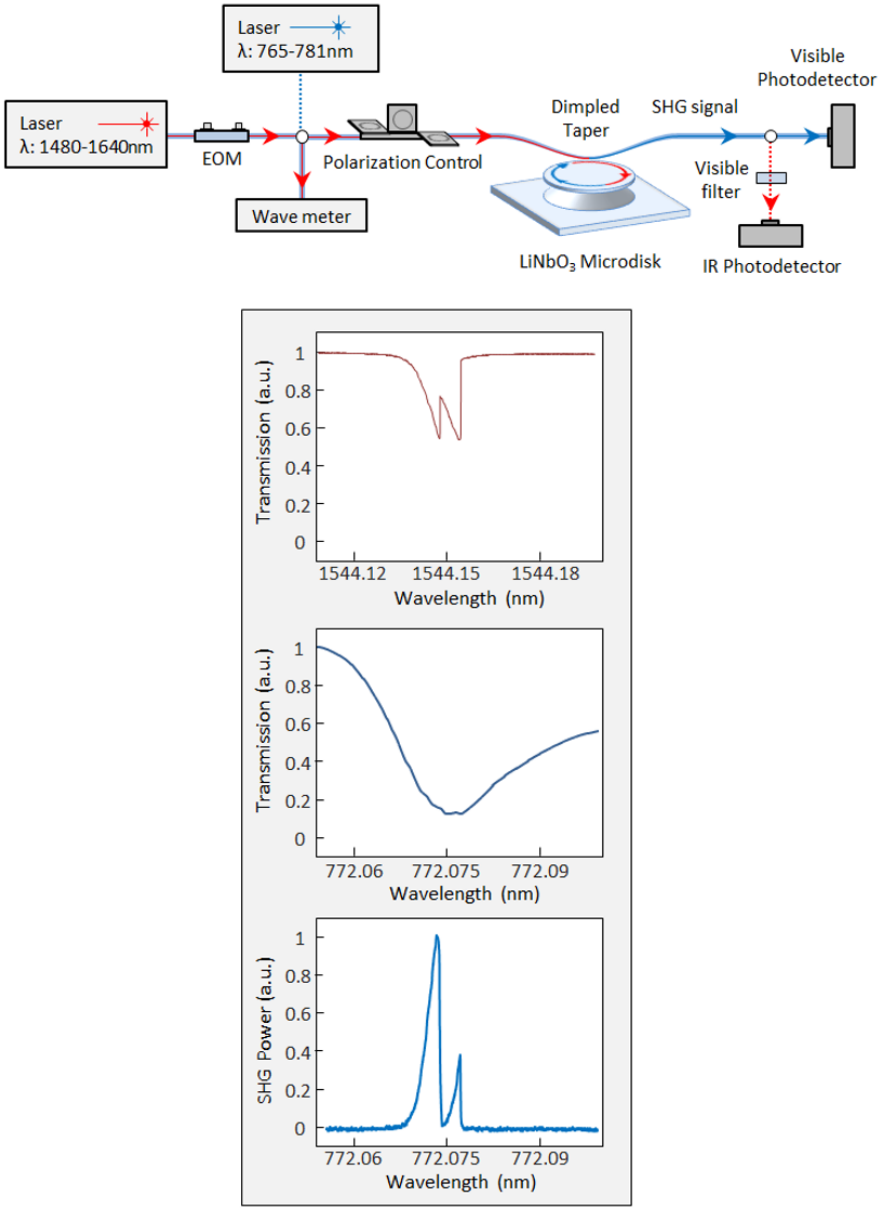

Figure 8. Second Harmonic Generation Phase Matching

To predict the conversion efficiency for doubly resonant SHG in the same microdisk, we adopt a coupled mode model similar to that developed in Ref 28. A major addition to our model is the inclusion of coherent backscattering (CBS) [33] of the pump. CBS is evident from the splitting of pump modes into resolved doublets (Fig. 8), and is represented in our model by the addition of two equations for the counter propagating modes. The coupled equations describing our system are:

$$\frac{da_{1,cw}}{dt} = (\,i\Omega_1 - \kappa_1)a_{1,cw} + \sqrt{2\,\kappa_{1,w}}s_{1,cw,+} + i\kappa_{BS}a_{1,ccw} + i\omega_1\beta_1 a_{1,cw}^{*}a_{2,cw} \tag{3}$$

$$\frac{da_{1,ccw}}{dt} = (\,i\Omega_1 - \kappa_1)a_{1,ccw} + i\kappa_{BS}a_{1,cw} + i\omega_1\beta_1 a_{1,ccw}^{*}a_{2,cw} \tag{4}$$

$$\frac{da_{2,cw}}{dt} = (\,i\Omega_2 - \kappa_2)a_{2,cw} + i\,\omega_2\beta_2\left|a_{1,cw}\right|^2 \tag{5}$$

$$\frac{da_{2,ccw}}{dt} = (\,i\Omega_2 - \kappa_2)a_{2,ccw} + i\omega_2\beta_2\left|a_{2,ccw}\right|^2 \tag{6}$$

where $a_{1,cw}$ and $a_{1,ccw}$ ($a_{2,cw}$ and $a_{2,ccw}$) are the complex cavity field amplitudes of the clockwise and counterclockwise circulating pump (SH) modes, normalized such that $|a|^2$ is the cavity energy in each mode; Ω_1 and Ω_2 are the frequency detuning of the pump and second harmonic from the cavity modes; κ_1 and κ_2 are the loss rates of the pump and second harmonic due to scattering, material absorption, and waveguide extraction; $\kappa_{1,w}$ and $\kappa_{2,w}$ are the loss rates due only to waveguide extraction; κ_{BS} is the rate of coherent backscattering of the pump mode; ω_1 and ω_2 are the angular frequencies of the pump and second harmonic; β_1 and β_2 are nonlinear coupling coefficients. They describe effective nonlinearities based on material nonlinearity and the spatial overlap of the modes, and their calculation is described in the supplement. The SH power extracted from the taper probe is $\left|\sqrt{2\,\kappa_{2,w}}\,a_{2,cw}\right|^2$.

We solve these equations numerically in steady-state (assuming that the time derivatives are zero), using the parameters extracted from transmission spectra (see supplement for details).
The same tapered fiber probe used to obtain transmission spectra is used to pump the microdisk at 1544 nm and extract the SH signal at 772 nm. The experimentally measured SH output power and efficiency are shown as a function of pump power, along with the values predicted by our model, in Figure 9. Reported values represent the internal conversion efficiency of the microdisk, with pump and SHG power calibrated to account for losses in the taper. Taper loss calibration is discussed in the next section.

The maximum output power at 772 nm achieved in our experiment is 256μW at a pump power of 3.14mW, or a conversion efficiency of 7.18%. This conversion efficiency is more than 20× the highest reported value in thin film $LiNbO_3$ at the same pump power [22].

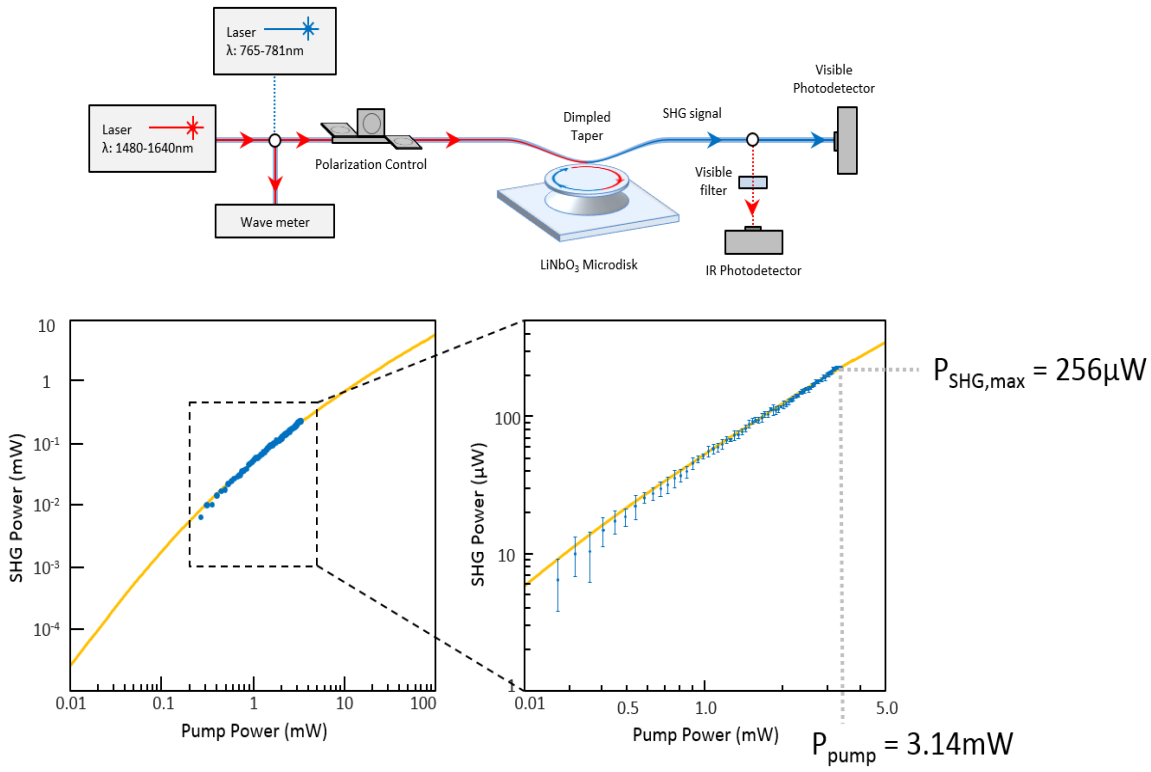

Figure 9. Second Harmonic Power vs Pump Power

As in Ref. 28, our model (Eq. 3-6) predicts a "critical" pump power, at which maximum conversion efficiency occurs (Fig. 10). The critical power for our system is 10.0 mW, with a conversion efficiency of 7.3%. However, above approximately 3 mW of pump power, we observe the onset of photorefractive damage. The SHG conversion efficiency is reduced, accompanied by a reduction in the resonator mode quality factors, changes which persist after reducing the pump intensity. Annealing the sample at 70°C for 30 minutes is sufficient to reverse the damage, but it is not possible to obtain reliable SHG results at higher pump powers due to the onset of damage. Doping the $LiNbO_3$ device layer with MgO should increase the optical damage threshold by a factor of approximately 100 [34], allowing us to easily reach the critical power, which has not yet been experimentally observed.

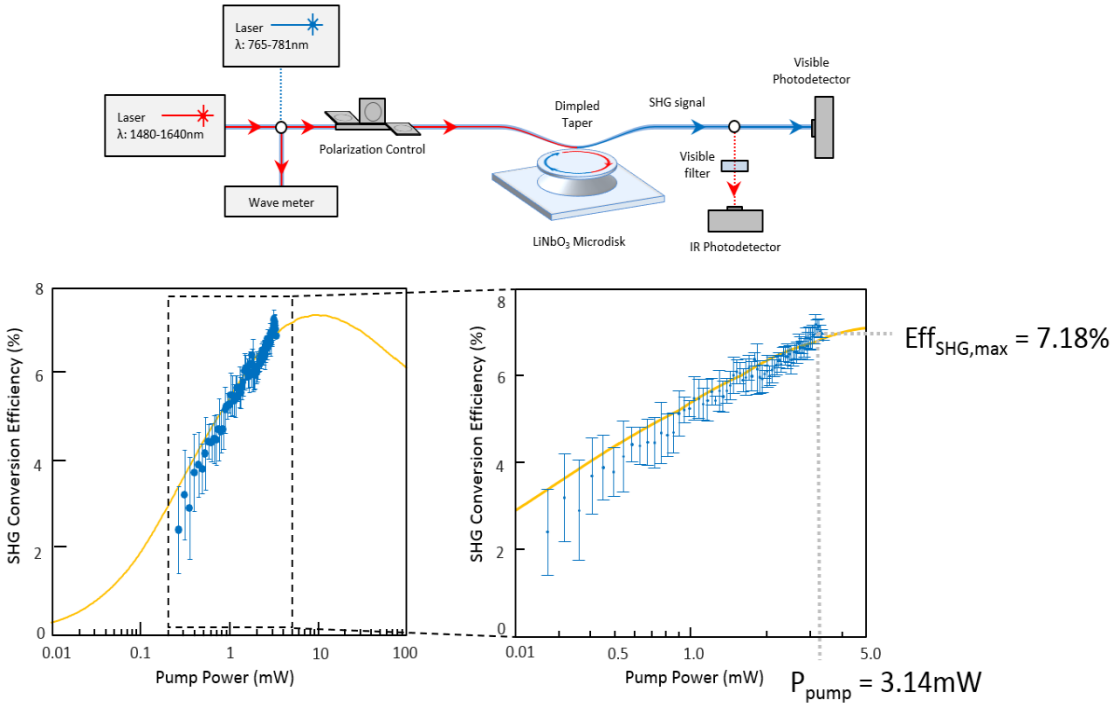

Figure 10. Second Harmonic Efficiency vs Pump Power

Our conversion efficiency and critical power are also limited by two separate considerations: coherent backscattering of the pump and inability to independently control the pump and signal waveguide loading rates. Reducing coherent backscattering of the pump to the material limit could produce a conversion efficiency of 7% at less than 100 μW of pump power. The use of a second taper probe or integrated waveguides to increase the pump loading rate could increase our SHG conversion efficiency to more than 20% at the same pump power. Details are discussed in the next section.

3.4 Spontaneous Parametric Down Conversion

The phase matching condition for degenerate SPDC is identical to that for SHG. We are therefore able to achieve a bright source of pair photons at λ_1 by changing the pump laser to the SH wavelength, λ_2. The damage threshold power at these wavelengths is considerably lower in this configuration leading to even stricter limits on available useful pump power. Once again, MgO doping should increase this threshold considerably [34].

As shown in Fig. 11, we see the characteristic linear pair production rate as a function of pump power as expected from SPDC [17]. Additionally, we confirm that pair generation is occurring

through coincidence counting. Fig 11 shows the expected coincidence spectrum as well as the measured spectrum.

The fringes in the spectrum are due to the doublet nature of the pump mode. The splitting apparent in the transmission scans around 1550 nm (see supplement) is attributable to the condition $\kappa_{BS} > \kappa_1$, meaning that photons at λ_1 are more likely to coherently backscatter into the counter-propagating mode than they are to decay out of the cavity. Because the λ_2 does not have this property, there is a negligible amount of power propagating counter to the pump. The phase matching condition for SPDC (and SHG) is only for co-propagating modes at the two wavelengths. This means that SPDC happens in a single direction. However, due to the relative rates of backscatter and decay, we see multiple fringes in the coincidence spectrum where one or both of the photons emerge from the microdisk traveling against the pump direction and are not counted. Further details of this interaction are still under investigation.

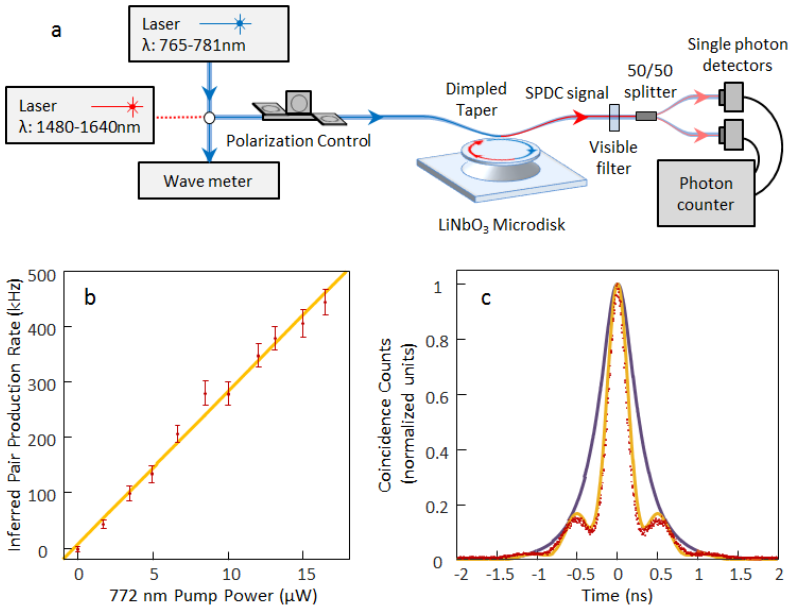

Figure 11. Spontaneous Parametric Down Conversion

3.4 Discussion

In this work, we present a novel phase matching technique for thin film nonlinear optical interactions. Our method, which we refer to as geometric birefringent phase matching, exploits geometric birefringence in the thin film to achieve perfect phase matching without periodic poling. Using this technique, we demonstrate second harmonic generation and spontaneous parametric down conversion in doubly resonant microdisks fabricated from thin film $LiNbO_3$. Pumping and extracting with a single tapered fiber probe, we show SHG at mW level pump powers, with more than 20× the efficiency of the best previous result in $LiNbO_3$ [22] and nearly identical to recently published results in aluminum nitride [27]. We also reverse the pump and

signal wavelengths to demonstrate spontaneous parametric down conversion, which has an identical phase matching condition, using the same microdisk.

These demonstrations represent an important step toward low power, chip-scale optical frequency synthesis. We believe that this demonstration, along with continuing advances in processing technology for thin film $LiNbO_3$ [23,35] can lead to novel architectures for fully integrated optical frequency synthesis, with important implications for frequency metrology and quantum information systems.

4. LNOI FREQUENCY CONVERSION – ADDITIONAL INFORMATION

4.1 Geometric Birefringent Phase Matching

Efficient nonlinear frequency conversion requires that the interacting waves maintain a fixed phase relationship. In general, normal material dispersion prevents phase matching. In thin films, however, phase matching can be realized by selecting orthogonal polarizations for the pump and signal modes. The differing electromagnetic boundary conditions for the two polarizations allow us to use geometric dispersion to compensate for material dispersion, satisfying the phase matching condition. We refer to this method as geometric birefringent phase matching (gBPM). We provide two examples of gBPM for second harmonic generation (SHG) in thin film $LiNbO_3$: the first is for a rectangular waveguide; the second is for a doubly resonant microdisk.

Rectangular Waveguide Example

In a rectangular, air-clad waveguide, the phase matching for SHG is simple: the effective index of the pump and signal modes must be equal. In $LiNbO_3$, which exhibits normal material dispersion, the bulk refractive index for 775 nm light is higher than the refractive index for 1550 nm light.

Figure 12 shows the effective index of the fundamental waveguide mode with λ_1 = 1550 nm and λ_2 = 775 nm, for each polarization, as a function of thickness, for a 1.5 μm wide waveguide made of z-cut, thin film $LiNbO_3$. The corresponding cross-sectional electric field profiles at waveguide thicknesses of 184 nm, 600 nm, and 1μm are shown in Fig. 12.

In a thick waveguide, the waveguide modes are strongly confined to the $LiNbO_3$, and the effective indices of the two modes approach their bulk indices. For thinner waveguides, the modes are forced outside the waveguide into the air, lowering their effective indices.

Because of the differing electromagnetic boundary conditions for light polarized perpendicular (TM) and parallel (TE) to the substrate, this effect is stronger for TM modes than for TE modes. The effective index for TM modes is therefore a stronger function of thickness than the effective index for TE modes. For thin waveguides, the effective index of a TM second harmonic mode can be lowered enough to equal the effective index of a TE pump mode, completely compensating for material dispersion.

For a TE pump mode and a TM second harmonic mode, the effective indices become equal at a thickness of 184 nm, as shown in Fig. 12a. A suspended thin film $LiNbO_3$ waveguide with a width of 1.5μm and a thickness of 184 nm can therefore be perfectly phase matched for SHG from 1550 nm to 775 nm using gBPM.

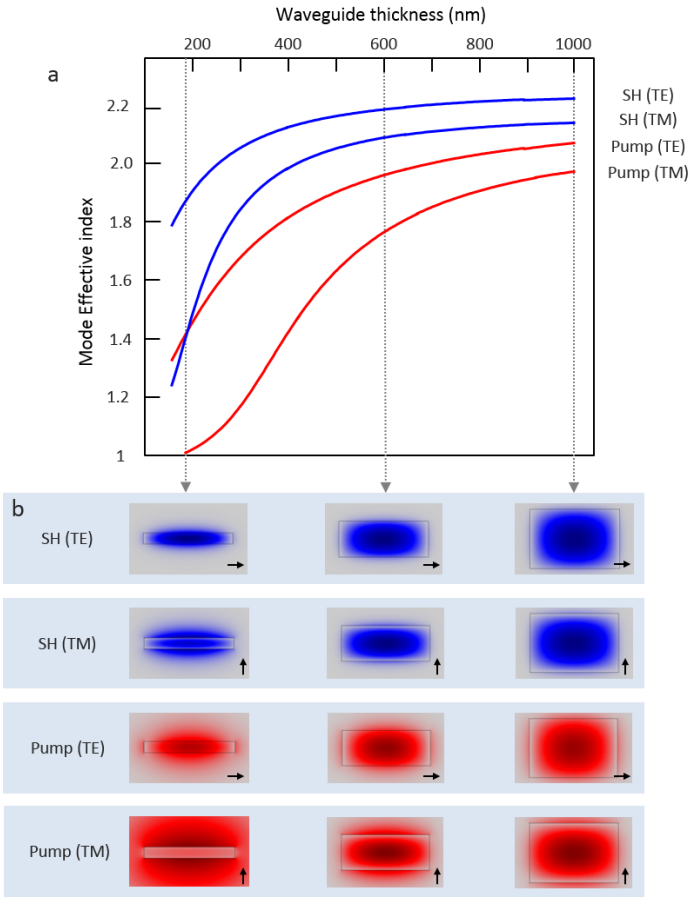

Figure 12. Geometric Birefringent Phase Matching in a Thin Film $LiNbO_3$ Waveguide

Microdisk Example

In a microdisk, the phase matching conditions for doubly resonant SHG are

$$2 \times m_1 - m_2 = \Delta m = 0 \tag{1}$$

$$2 \times f_1 - f_2 = \Delta f = 0$$
$$(2 \times \lambda_2 - \lambda_1 = \Delta\lambda = 0) \tag{2}$$

where m_1 and m_2 the azimuthal mode orders of the pump and SHG mode, respectively, and f_1 and f_2 are the resonant eigenfrequencies of the pump and SH mode, respectively. ΔM and $\Delta f(\Delta\lambda)$ represent momentum and energy mismatch between the pump and SHG modes, and are zero for perfect phase matching. This condition is less intuitive, but is analogous to, the phase matching condition for the rectangular waveguide.

Figure 13a shows f_1 and f_2 for the fundamental resonator mode with $m_1 = 121$ and $m_2 = 242$, for each polarization, as a function of thickness, for a 20.016 μm radius microdisk made of z-cut,

thin film $LiNbO_3$. The corresponding cross-sectional electric field profiles at waveguide thicknesses of 189 nm, 600 nm, and 1μm are shown in Fig. 13b.

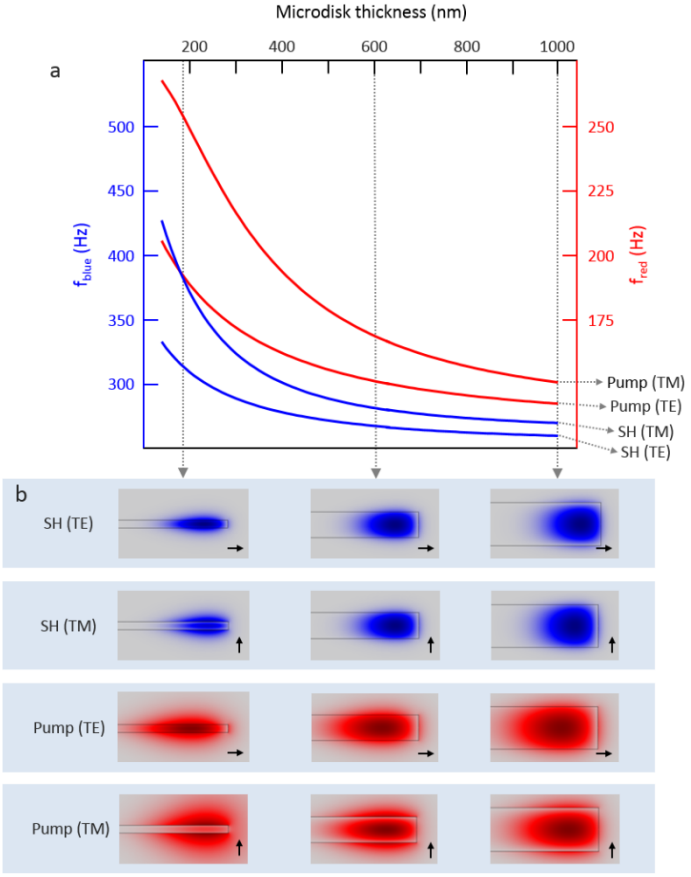

Figure 13. Geometric Birefringent Phase Matching in a Thin Film $LiNbO_3$ Microdisk

Similar to the case for the waveguide, for a thick microdisk, normal material dispersion prevents phase matching. The resonator modes are confined strongly to the disk, and $\Delta f > 0$. As for the waveguide case, for a thin disk, gBPM can be used to cancel material dispersion. For a TM second harmonic mode and a TE pump mode, $\Delta f = 0$ for a microdisk thickness of 189.4 nm. The corresponding pump and SH wavelengths for the two resonator modes are 1544.16 nm and 772.08 nm. Doubly resonant SHG is therefore possible using these two cavity modes.

In both the case of the waveguide and the resonator, it should be noted that the phase matching condition for degenerate spontaneous parametric down conversion (SPDC) is identical to the phase matching condition for SHG. A structure where gBPM is used to phase match SHG will then also be valid for phase matched SPDC.

Compensation for Microdisk Thickness Variation

In order to account for local thickness variation in the LNOI wafers, the phase matching analysis is repeated for the actual thickness of each sample. In Fig. 14, we plot Δf as a function of radius

for several adjacent m_1/m_2 pairs for our actual disk thickness of 189.4 nm. Each x-intercept gives the radius for a phase matched disk, with a corresponding pair of pump and SH wavelengths, plotted in S3. We find that a microdisk with radius 20.016μm is phase matched, with the following values: $m_1 = 121$, $m_2 = 242$; $f_1 = 194.15$ THz ($\lambda_1 = 1544.15$ nm), $f_2 = 388.29$ THz ($\lambda_2 = 772.075$ nm).

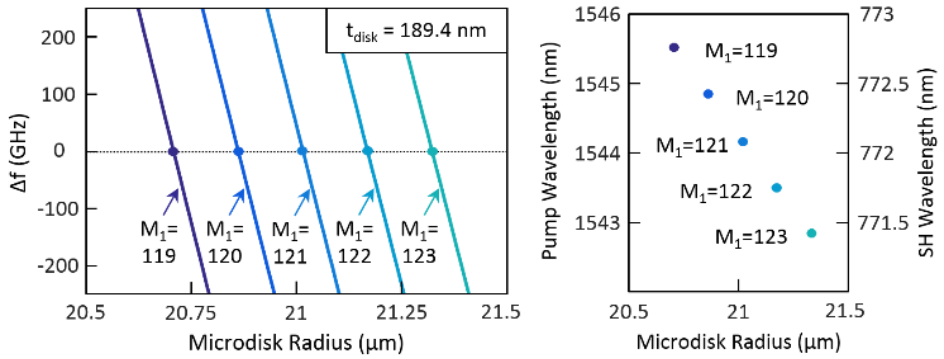

Figure 14. Geometric Birefringent Phase Matching for 189.4nm Thickness Lithium Niobate Microdisk

4.2 Microdisk Quality Factor, Loss Rates

Microdisk whispering gallery mode quality factors are calculated from transmission spectra, using the experimental configuration shown in Fig. 15. The same tapered fiber probe is used for 1550 nm and 775 nm characterization. High Q resonator modes in the 1550 nm range show a doublet structure due to coherent backscattering, and are fit with the expression:

$$T = \left| 1 + \frac{2\,\kappa_w (i(\omega - \omega_0) - \kappa_w - \kappa_i)}{\kappa_{BS}^2 + (i(\omega - \omega_0) - \kappa_w - \kappa_i)^2} \right|^2$$

where κ_i and κ_w are the intrinsic and waveguide loss rates, respectively, and κ_{BS} is the rate of coherent backscattering. The intrinsic resonator quality factor is

$$Q_i = \frac{\omega}{\kappa_i}$$

The highest quality factors measured in our LNOI microdisks were 575,000 (1550 nm) and 75,500 (775 nm). The corresponding transmission spectra and fits are shown in Fig. 15.

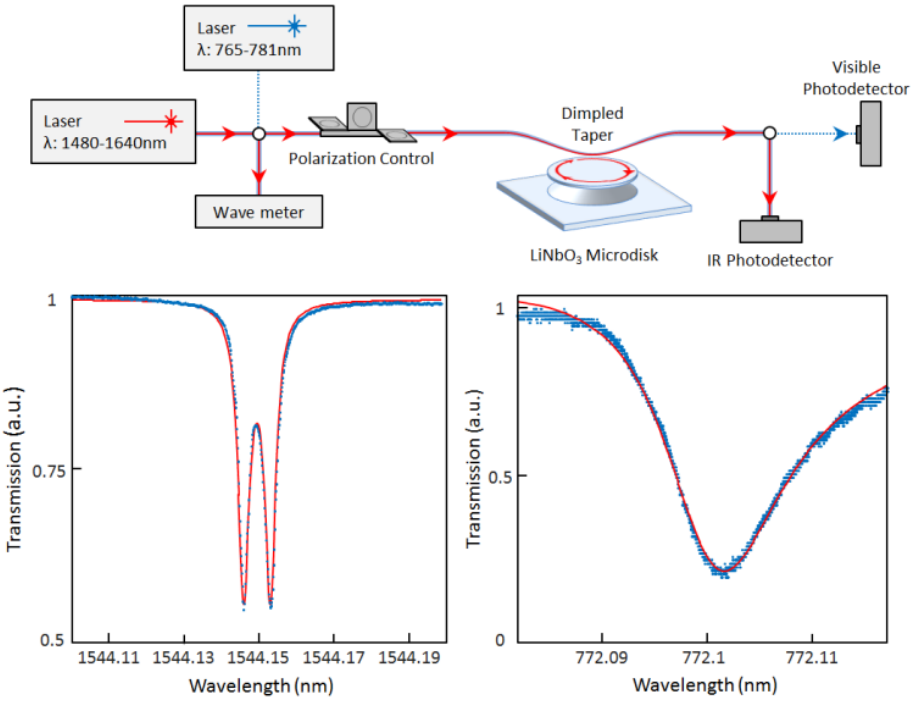

Figure 15. Microdisk Quality Factor Measurement

The values used to model the SH power and efficiency in the main text were extracted using the same expressions. However, we were unable to accurately determine the waveguide loading rate for the pump wavelength during SHG. Mechanical instability of the taper probe over the time required to move fiber connections and change the laser power caused the position of the taper to drift, changing the loading rate significantly. κ_w was therefore used as a fit parameter for the coupled mode model, constrained within the experimentally observed values for the pump resonator mode.

4.3 SHG Model Parameters

The following parameters for the SHG model were extracted from the transmission spectra using the experimental configuration in Fig. 15.

$\Omega_1 = \Omega_2 = 0$, κ_1 =1.77 GHz, κ_2 = 42.9 GHz, $\kappa_{1,w}$ = 0.71 GHz, $\kappa_{2,w}$ = 13.6 GHz, κ_{BS} = 2.86 GHz
ω_1 = 1.22×10^{15} rad/s, ω_2 = 2.44×10^{15} rad/s

The SHG power/efficiency data was then collected without moving the tapered fiber probe, in order to ensure correspondence of the model with the experimental system.

Nonlinear coupling coefficients (β) were calculated according to [Johnson], using the following expressions:

$$\beta_1 = \frac{1}{4}\frac{\int d^3x \sum_{ijk\epsilon} \chi^{(2)}_{ijk} \left[E^*_{1i}(E_{2j}E^*_{1k} + E^*_{1j}E_{2k})\right]}{\left[\int d^3x \epsilon |\boldsymbol{E}_1|^2\right]\left[\int d^3x \epsilon |\boldsymbol{E}_2|^2\right]^{1/2}}$$

$$\beta_2 = \frac{1}{4}\frac{\int d^3x \sum_{ijk\epsilon} \chi^{(2)}_{ijk} E^*_{2i}E_{1j}E_{1k}}{\left[\int d^3x \epsilon |\boldsymbol{E}_1|^2\right]\left[\int d^3x \epsilon |\boldsymbol{E}_2|^2\right]^{1/2}}$$

In order to calculate $\beta_1$and β_2, we use the same 2D axisymmetric model described in the main text to solve for the eigenmodes of our resonator. A microdisk with thickness 189.4 nm and radius 21.016 μm, with $m_1 = 121$ ($m_2 = 242$) was simulated. The TE pump mode and TM second harmonic mode wavelengths were found to be 1544.16 and 772.08 nm. The corresponding electric field profiles were numerically integrated to calculate β_1 = 20.29 - 0.00053i $1/\sqrt{Joule}$ and β_2 =10.14 + 0.00026i $1/\sqrt{Joule}$.

4.4 Taper Loss Calibration

Here we calculate the transmission coefficient for the taper at each wavelength, from each side, to account for loss of optical power in the taper. The results for SHG and SPDC power and efficiency presented in the main text represent the internal conversion efficiency of the microdisk, with the pump and signal powers scaled by the appropriate transmission coefficients for each experiment.

In order to calculate the taper transmission coefficients, we first measure the taper transmission at λ_1 and λ_2. $T_{1,\ total}$ = 9.2% and $T_{2,\ total}$ = 9.2% If the taper loss is symmetric, then the transmission to/from the microdisk from either side of the taper is simply the square root of the total transmission, e.g. $T_{1,\ left}$ = 30.3%

However, the losses for each wavelength are not necessarily symmetric. In order to calculate the relative loss from each side at λ_1, we first identify an observable, power-dependent effect in the resonator: a change in the resonance shape due to thermal bistability. We then measure the ratio of the laser power required to achieve the same amount of resonance distortion when pumping from the left or the right:

$$\frac{P_{1,left}}{P_{1,right}} = 1.5849$$

$$\frac{P_{2,left}}{P_{2,right}} = 0.4875$$

The single sided transmission of the taper at each wavelength can then be calculated:

$$T_{1,left} = \sqrt{T_{1,total}\frac{P_{1,right}}{P_{1,left}}} = 0.240$$

$$T_{1,right} = \sqrt{T_{1,total}\frac{P_{1,left}}{P_{1,right}}} = 0.381$$

$$T_{2,left} = \sqrt{T_{2,total}\frac{P_{2,right}}{P_{2,left}}} = 0.424$$

$$T_{2,right} = \sqrt{T_{2,total}\frac{P_{2,left}}{P_{2,right}}} = 0.207$$

4.5 Improving System Performance

There are several possible improvements to the system which can increase the SHG conversion efficiency and/or lower the "critical" power at which maximum conversion efficiency occurs. In addition to increasing the intrinsic quality factors of the modes and raising the optical damage threshold, we have identified two important ways to improve the system performance: 1) Increase the loading rate of the pump waveguide and 2) reduce the rate of coherent backscattering of the pump. Using the measured system parameters discussed in the main text, we use our coupled mode model to predict the system performance if these parameters can be improved.

Pump Waveguide Loading Rate

The use of a single taper for pump and signal is convenient, but it does not allow for independent control of the waveguide loading rates $\kappa_{1,w}$ and $\kappa_{2,w}$. In particular, the pump mode is undercoupled in the results presented in the main text. Figure 16 shows the SHG conversion efficiency, calculated from our coupled mode model, if $\kappa_{1,w}$ is increased, while holding all other parameters constant. If the pump loading rate is increased from 1 GHz to 7 GHz, the maximum conversion efficiency increases from 7.3% to 25% (at the cost of slightly increasing the critical power). We can easily achieve values this high for $\kappa_{1,w}$ if the position and diameter of the taper are optimized for the pump, but the use of a single taper prohibits independently optimizing the waveguide loading rate for each mode.

Independent control of the waveguide loading rates can be achieved either by using multiple tapers or integrated waveguides.

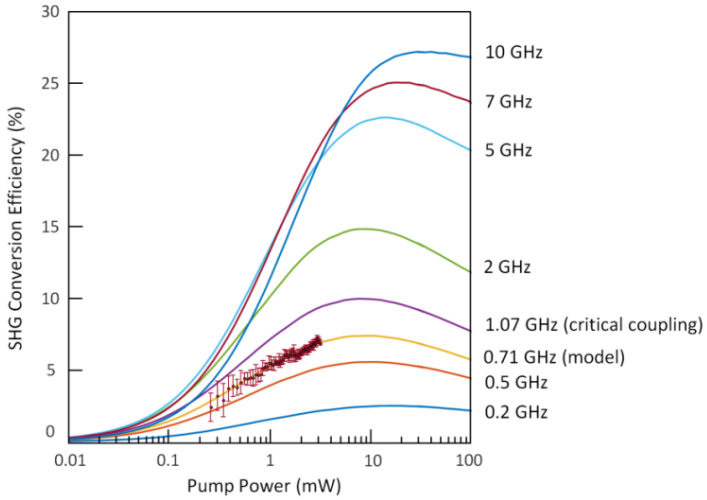

Figure 16. SHG Conversion Efficiency for Different Pump Waveguide Loading Rates

Coherent Backscattering Rate

Although coherent backscattering of the 1550 nm microdisk whispering gallery modes leads to interesting dynamics for SPDC photon timing correlations, it represents a loss mechanism with respect to both SHG and SPDC conversion efficiency. In Figure 17, we again use our coupled mode model to predict the system SHG performance if the backscattering rate κ_{BS} is lowered.

The measured value of κ_{BS} for our SHG pump mode is 2.86 GHz. Reducing κ_{BS} to 100 MHz would increase the conversion efficiency from 7.2% to 12.5% and decrease the critical pump power from 10 mW to 1.1 mW. Reducing κ_{BS} further has little effect on the efficiency or critical power. The material limit for the coherent backscattering rate in $LiNbO_3$ has previously been estimated to be 10 MHz, so 100MHz represents a conservatively achievable value.

Reducing κ_{BS} requires a reduction of the microdisk sidewall roughness, which is a fabrication challenge. Improved etching of the resonator sidewalls could decrease the sidewall roughness. Additionally, there have been demonstrations of decreased sidewall roughness via high temperature reflow of the microdisk surface, although this method poses additional challenges for integration.

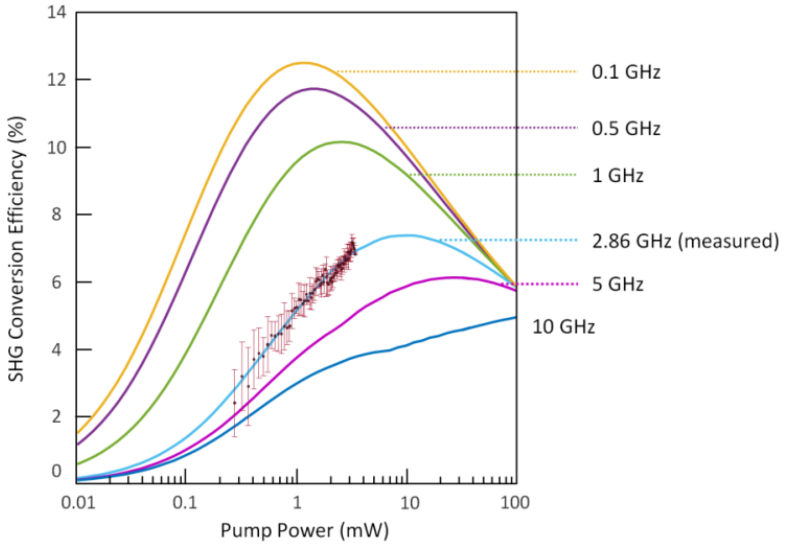

Figure 17. SHG Conversion Efficiency for Different Coherent Backscattering Rates

5. ELECTRO-OPTIC MODULATION

In addition to applications in nonlinear optics, $LiNbO_3$ is also a standard material for electro-optics. In this section, we demonstrate the electro-optic modulation of resonator modes in thin film microdisks produced using fabrication techniques similar to those described in the previous two sections. An electric field applied between a probe placed above the disk and a metal plane integrated into the LNOI substrate modifies the resonator refractive index, resulting in a displacement of the optical mode.

5.1 Fabrication

Z-cut lithium niobate wafers were obtained commercially from Nanoln. The wafers consisted of a top 400nm thick crystalline z-cut lithium niobate layer on top of a 2um silicon dioxide layer and a 30nm chromium / 100nm gold / 10nm chromium metal layer, all on top of a z-cut lithium niobate handle wafer. Microdisk optical resonators were defined by ebeam lithography using ZEP520A as the resist. The disks were etched using a simple argon ion beam using the resist layer as the etch mask. The devices were then undercut using a benchtop vapor hydrofluoric acid process leaving undercut lithium niobate disks attached by an oxide pedestal to the underlying metal layer. This process is illustrated in Figure 18.

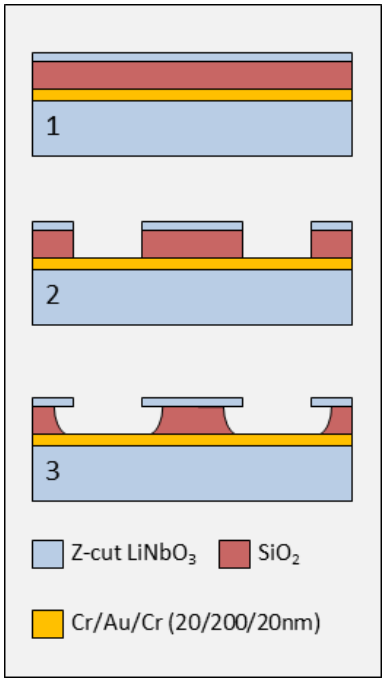

Figure 18. Process Flow for $LiNbO_3$ Electro-Optic Structures

An optical micrograph of a fabricated microdisk is shown in Figure 19. The metal plane is exposed in the area around the disk, allowing contact with an electrical probe, as shown in Figure 20.

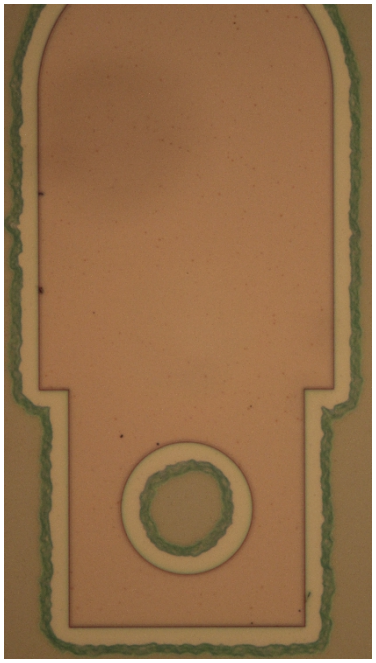

Figure 19. Fabricated $LiNbO_3$ Electro-Optic Microdisk

5.2 Experimental Results

Optical modes of the microdisk resonators are interrogated using the tapered fiber probe described in previous sections. Applying an electrical potential between a metal probe placed above the microdisk and the metal ground plan integrated into the substrate (Figure 20), we produce a refractive index change in the microdisk via the electro-optic effect. This index change results in a lengthening or shortening of the effective resonator circumference, depending on the sign of the applied voltage, shifting the wavelength of the optical resonator modes.

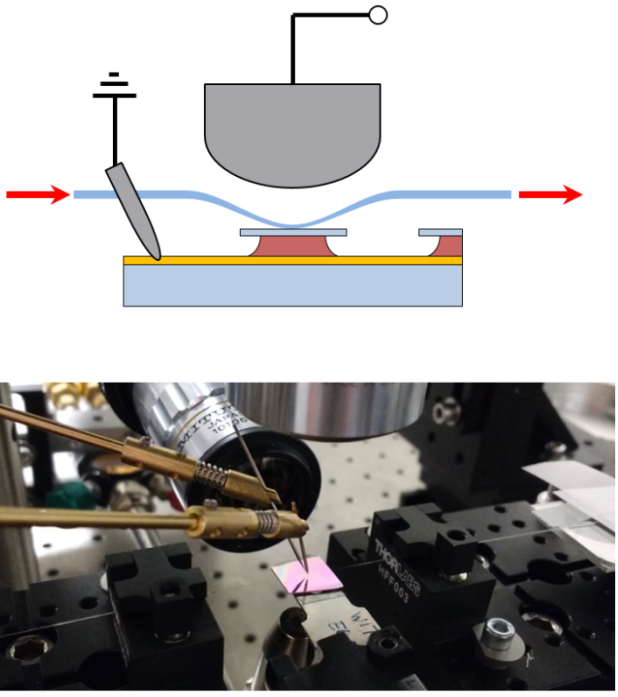

Figure 20. Measurement Apparatus for $LiNbO_3$ Electro-Optic Microdisk

The displacement of the resonator modes ($\Delta\lambda$) is plotted as a function of the applied voltage (ΔV) in Figure 21. Two separate modes are evaluated for each optical polarization. Optical modes polarized perpendicular to the substrate (TM) experience a larger shift than modes polarized parallel to the substrate (TE), due to the difference in the relevant components of the electro-optic tensor ($r_{33} > r_{31}$).

Also plotted in Figure 21 are the results of a finite element method model which predicts our system's behavior. The lines plotted assume a 20 μm gap between the top electrode and the microdisk surface, and the microdisk dimension modeled are identical to the measured dimensions of the disks corresponding to the experimental data.

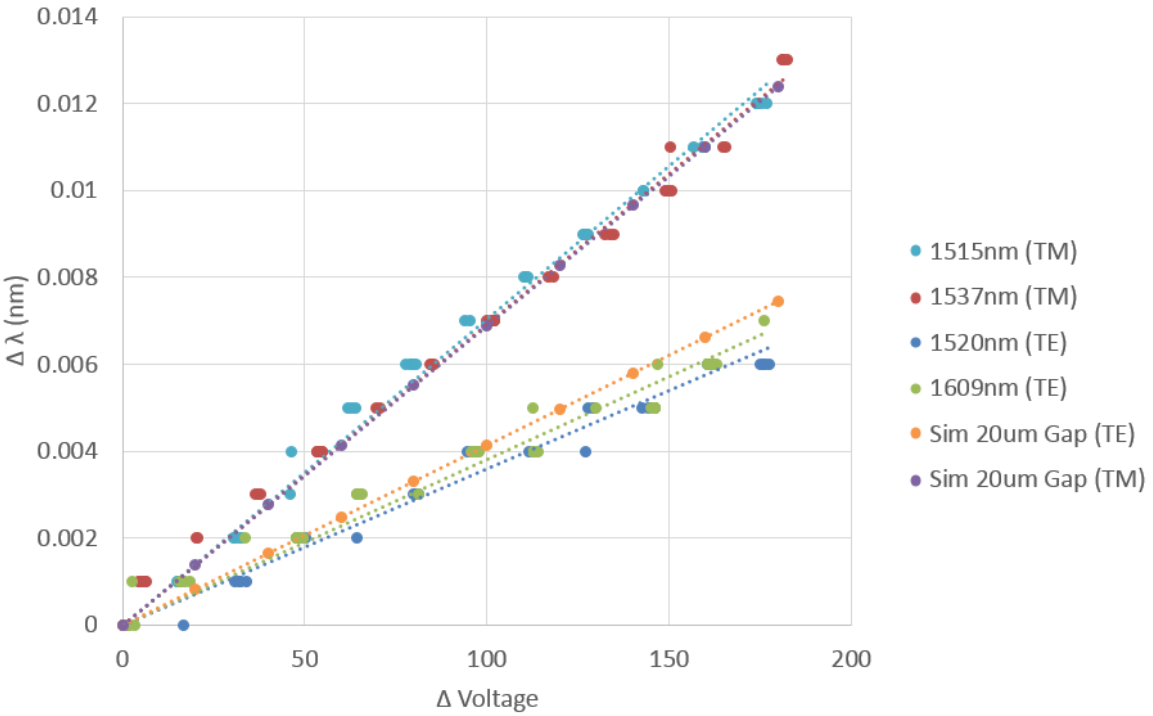

Figure 21. Microdisk Resonance Wavelength Shift vs Applied Voltage

5.2 Discussion

This demonstration of electro-optic modulation in thin film $LiNbO_3$ microdisks represents a first step toward creating more efficient amplitude and phase modulators, as well as modulators integrated with other photonic systems. Thin film structures offer tight confinement of light and can be routed for long distances on a chip. Metalized LNOI wafers provide a platform for realizing novel electro-optic device architectures at the chip scale.

6. CONCLUSION

In this report, we have described work done under the LDRD program at Sandia National Laboratories to produce reduced dimensionality lithium niobate microsystems. We have demonstrated two methods for fabricating thin film $LiNbO_3$ suspended structures. The first, based on ion implantation of a bulk substrate, was used to produce optical microdisk resonators from a commercial bulk $LiNbO_3$ wafer. The second approach used commercial $LiNbO_3$ on insulator (LNOI) wafers. Although this process relies on more expensive substrates, the devices produced from this material show much lower surface roughness and correspondingly higher optical quality factors. Using thin film microdisks, we demonstrate optical second harmonic generation and spontaneous parametric down conversion with state-of-the-art efficiency, as well as electro-optic modulation.

.

7. REFERENCES

1. Udem, Th., Holzwarth, R. and Hänsch, T.W. Optical frequency metrology. *Nature* 416, 233-237 (2002).
2. Cundiff, S.T. and Ye, J. Colloquium: Femtosecond optical frequency combs. *Rev. Mod. Phys.* **75**, 325 (2003).
3. Kippenberg, T.J., Holzwarth, R., Diddams, S.A. Microresonator-Based Optical Frequency Combs. *Science* **332**, 555 (2011).
4. De Greve, K., Yu, L., McMahon, P.L., Pelc, J.S., Natarajan, C.M., Kim, N.Y., Abe, E., Maier, S., Schneider, C., Kamp, M., Ho¨fling, S., Hadfield, R.H., Forchel, A., Fejer, M.M., and Yamamoto, Y. Quantum-dot spin–photon entanglement via frequency downconversion to telecom wavelength. *Nature* **491**, 421 (2012).
5. Ma, L., Slattery, O., Tang, X. Single photon frequency up-conversion and its applications. *Phys. Rep.* **521**, 69–94 (2012).
6. Tanzilli, S., Martin, A., Kaiser, F., De Micheli, M.P., Alibart, O., and Ostrowsky, D.B. On the genesis and evolution of Integrated Quantum Optics. *Laser & Photon. Rev.* **6**, 115 (2011).
7. Ramelow, S., Farsi, A., Clemmen, S., Orquiza, D., Luke, K., Lipson, M., Gaeta, A.L. Silicon-Nitride Platform for Narrowband Entangled Photon Generation. *arXiv:1508.04358* [quant-ph] (2015).
8. Camacho, R.M. Entangled photon generation using four-wave mixing in azimuthally symmetric microresonators. *Opt. Express* **20**, 21977-21991 (2012).
9. Azzini, S., Grassani, D., Strain, M.J., Sorel, M., Helt, L.G., Sipe, J.E., Liscidini, M., Galli, M., and Bajoni, D. Ultra-low power generation of twin photons in a compact silicon ring resonator. *Opt. Express* **20**, 23100-23107 (2012).
10. Tanzilli, S., Tittel, W., De Riedmatten, H., Zbinden, H., Baldi, P., DeMicheli, M., Ostrowsky, D.B., Gisin, N., PPLN waveguide for quantum communication. *Eur. Phys. J. D* **18**, 155 (2002).
11. Takesue, H., Inoue, K., Tadanaga, O., Nishida, Y., and Asobe, M. Generation of pulsed polarization-entangled photon pairs in a 1.55-μm band with a periodically poled lithium niobate waveguide and an orthogonal polarization delay circuit. *Opt. Lett.* **30**, 293-295 (2005).
12. Arizmendi, L. Photonic applications of lithium niobate crystals. *phys. stat. sol. (a)* **201**, 2, 253–283 (2004).
13. Ilchenko, V.S., Savchenkov, A.A., Matsko, A.B., and Maleki, L. Nonlinear Optics and Crystalline Whispering Gallery Mode Cavities. *Phys. Rev. Lett.* **92**, 043903 (2004).
14. Fürst, J.U., Strekalov, D.V., Elser, D., Aiello, A., Andersen, U.L., Marquardt, Ch., and Leuchs, G. Naturally Phase-Matched Second-Harmonic Generation in a Whispering-Gallery-Mode Resonator. *Phys. Rev. Lett.* **105**, 263904 (2010).
15. Savchenkov, A.A., Matsko, A.B., Mohageg, M., Strekalov, D.V., and Maleki, L. Parametric oscillations in a whispering gallery resonator. *Opt. Lett.* **32**, 157-159 (2007).

16. Moore, J., Tomes, M., Carmon, T., and Jarrahi, M. Continuous-wave ultraviolet emission through fourth-harmonic generation in a whispering-gallery resonator. *Opt. Exp.* **19**, 24139-24146 (2011).
17. Förtsch, M., Fürst, J.U., Wittmann, C., Strekalov, D., Aiello, A., Chekhova, M.V., Silberhorn, C., Leuchs, G., and Marquardt, C. A versatile source of single photons for quantum information processing. *Nat. Comm.* **4**, 1818 (2013).
18. Förtsch, M., Schunk, G., Fürst, J.U., Strekalov, D., Gerrits, T., Stevens, M.J., Sedlmeir, F., Schwefel, H.G.L., Nam, S.W., Leuchs, G., and Marquardt, C. Highly efficient generation of single-mode photon pairs from a crystalline whispering-gallery-mode resonator source. *Phys. Rev. A* 91, 023812 (2015).
19. Wang, R. and Bhave, S.A. Free-standing high quality factor thin-film lithium niobate micro-photonic disk resonators. *arXiv:1409.6351* [physics.optics] (2014).
20. Chauvet, M., Henrot, F., Bassignot, F., Devaux, F., Gauthier-Manuel, L., Pêcheur, V., Maillotte, H., Dahmani, B., LiNbO3 ridge waveguides realized by precision dicing on silicon for high efficiency second harmonic generation. *arXiv:1603.05267* (2016).
21. Wang, C., Burek, M.J., Lin, Z., Atikian, H.A., Venkataraman, V.,Huang, I.C., Stark, P., and Lončar, M. Integrated high quality factor lithium niobate microdisk resonators. *Opt. Exp. 22*, 30924-30933 (2014).
22. Lin, J., Xu, Y., Fang, Z., Wang, M., Fang, W., Cheng, Y. Efficient second harmonic generation in an on-chip high-Q crystalline microresonator fabricated by femtosecond laser. *Proc. SPIE 9727, Laser Resonators, Microresonators, and Beam Control XVIII*, 972710 (2016).
23. Rabiei, P., Ma, J., Khan, S., Chiles, J., and Fathpour, S. Heterogeneous lithium niobate photonics on silicon substrates. *Opt. Express* **21**, 25573-25581 (2013).
24. Lake, D.P., Mitchell, M., Jayakumar, H., dos Santos, L.F., Curic, D., and Barclay, P.E. Efficient telecom to visible wavelength conversion in doubly resonant gallium phosphide microdisks. *Appl. Phys. Lett.* **108**, 031109 (2016).
25. Pernice, W.H.P., Xiong, C., Schuck, C., and Tang, H.X. Second harmonic generation in phase matched aluminum nitride waveguides and micro-ring resonators. *Appl. Phys. Lett.* **100**, 223501 (2012).
26. Kuo, P.S., Bravo-Abad, J., and Solomon, G.S. Second-harmonic generation using quasi-phasematching in a GaAs whispering-gallery-mode microcavity. *Nat. Com*. **5**, 3109 (2014).
27. Rodriguez, A., Soljačić, M., Joannopoulos, J.D., and Johnson, S.G. $\chi(2)$ and χ (3) harmonic generation at a critical power in inhomogeneous doubly resonant cavities. *Opt. Exp.* **15**, 7303-7318 (2007).
28. Guo, X., Zou, C.-L., and Tang, H.X. Second-harmonic generation in aluminum nitride microrings with 2500%/W conversion efficiency. Optica **3**, 1126-1131 (2016).
29. Yang, K.Y., Beha, K., Cole, D.C., Yi, X., Del'Haye, P., Lee, H., Li, J., Oh, D.Y., Diddams, S.A., Papp, S.B., and Vahala, K.J. Broadband dispersion-engineered microresonator on a chip. *Nat. Phot.* **10**, 316–320 (2016).
30. Boyd, R. *Nonlinear Optics*, 3rd ed. (Academic Press, 2008).

31. Michael, C.P., Borselli, M., Johnson, T.J., Chrystal, C., and Painter, O. An optical fiber-taper probe for wafer-scale microphotonic device characterization. *Opt. Exp.* **15** (8) 4745 (2007).
32. Bryan, D.A., Gerson, R., Tomaschke, H.E. Increased optical damage resistance in lithium niobate. *Appl. Phys. Lett.* **44** (9), 1984.
33. Hauer, B.D., Kim, P.H., Doolin, C., MacDonald, A.J.R., Ramp, H., and Davis, J.P. On-chip cavity optomechanical coupling. *EPJ Tech. Instrum.* **1**, 4 (2014).
34. Weiss, D.S., Sandoghdar, V., Hare, J., Lef`evre-Seguin, V., Raimond, J.-M. , and Haroche, S. Splitting of high-Q Mie modes induced by light backscattering in silica microspheres. *Opt. Lett*. **20** (18), 1835 (1995).
35. Weigel, P.O., Savanier, M., DeRose, C.T., Pomerene, A.T., Starbuck, A.L., Lentine, A.L., Stenger, V., and Mookherjea, S. Lightwave Circuits in Lithium Niobate through Hybrid Waveguides with Silicon Photonics. *Sci. Reports* **6**, 22301 (2016).

DISTRIBUTION

4 Lawrence Livermore National Laboratory
Attn: N. Dunipace (1)
P.O. Box 808, MS L-795
Livermore, CA 94551-0808

1	MS0161	Legal Technology Transfer Center	11500
1	MS0359	D. Chavez, LDRD Office	1911
1	MS0899	Technical Library	9536 (electronic copy)


Sandia National Laboratories